ELSEVIER

Contents lists available at ScienceDirect

Chinese Journal of Physics

journal homepage: www.sciencedirect.com/journal/chinese-journal-of-physics





Thermal and computational analysis of MHD dissipative flow of Eyring–Powell fluid: Non-similar approach via overlapping grid-based spectral collocation scheme

Muhammad Idrees Afridi ^{a,b,*}, M.P. Mkhatshwa ^{c,*}, Muhammad Qasim ^{d,*}, Ali J. Chamkha ^e

- ^a School of Mathematics and Computer Science, Hanjiang Normal University, Shiyan 442000, China
- ^b Applied Science Research Center, Applied Science Private University, Amman, Jordan
- ^c Department of Mathematics and Applied Mathematics, University of Limpopo, Private Bag X1106, Sovenga, 0727, South Africa
- ^d Department of Mathematics, COMSATS University Islamabad (CUI) Park Road, Tarlai Kalan, Islamabad 45550
- ^e Faculty of Engineering, Kuwait College of Science and Technology, Doha District, 35004, Kuwait

ARTICLE INFO

Keywords: Thermal analysis Numerical simulation Eyring Powell fluid Non-similar solutions Overlapping grid-based spectral collocation scheme Viscous dissipation

ABSTRACT

The aim of the present study is to numerically investigate the non-similar flow and heat transfer in a dissipative Eyring-Powell fluid (EPF) over a stretching surface. A constant magnetic field is applied perpendicular to the stretched surface to explore the impact of the Lorentz force. Both viscous and magnetic dissipation are considered to comprehensively examine their effects on heat transfer. The problem in hand does not admit self-similar solutions as the non-Newtonian fluid parameter varies with the spatial variable along the stream-wise direction. Consequently, the set of nonlinear partial differential equations, modeling the flow problem is nondimensionalized primarily by employing a pseudo-similarity variable and stream-wise coordinate. The nondimensional set of nonlinear partial differential equations is solved by a newly developed and efficient "overlapping multi-domain bivariate spectral local linearization method (OMD-BSLLM)". The current study includes residual error analysis and convergence tests to demonstrate the accuracy of the numerical method applied to the current mathematical model. Graphs show fluid flow and heat transfer results for different flow parameters, while tables display skin friction and Nusselt number values. The results indicate that the non-Newtonian fluid parameter enhances both the velocity profile and temperature distribution. The fluid decelerates with increasing the dimensionless stream wise coordinate and Hartmann number. Viscous dissipation and dimensionless stream-wise coordinate enhances the temperature profile.

1. Introduction

Estimation of heat transfer rates and shear stress in flows of non-Newtonian fluids are of considerable practical importance across diverse engineering and industrial sectors. Non-Newtonian fluids, characterized by their deviation from Newton's law of viscosity, that is, the principal feature exhibited by non-Newtonian fluids pertains to the non-linear correlation observed between shear stress and shear rate. Non-Newtonian fluids are categorized by their shear rate response, encompassing shear-thinning and shear-thickening

E-mail addresses: afridi@hjnu.edu.cn (M.I. Afridi), patsonmkhatshwa@gmail.com (M.P. Mkhatshwa), mq_qau@yahoo.com (M. Qasim).

https://doi.org/10.1016/j.cjph.2024.09.035

Received 18 July 2024; Received in revised form 22 September 2024; Accepted 24 September 2024 Available online 27 September 2024

0577-9073/© 2024 The Physical Society of the Republic of China (Taiwan). Published by Elsevier B.V. All rights are reserved, including those for text and data mining, AI training, and similar technologies.

^{*} Corresponding authors.

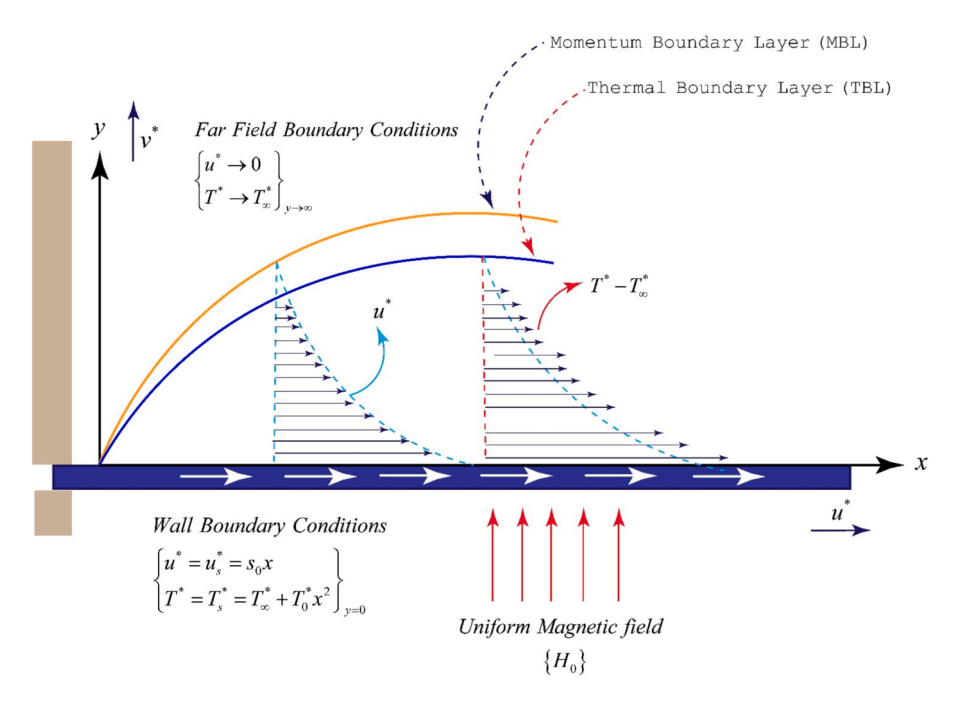


Fig. 1. Flow configuration.

fluids, as well as viscoelastic fluids. Some exhibit time-dependent behavior, such as thixotropic or rheopectic characteristics, while others are classified by stress dependency, with yield stress fluids necessitating a threshold stress for flow initiation. Fundamental challenge in the theoretical exploration of non-Newtonian fluid mechanics and the precise interpretation of experimental observations stems from the lack of a universal relationship between the stress and the deformation tensor applicable to all fluids [1-4]. Consequently, different models of non-Newtonian fluid have been established with the aim of capturing the diverse characteristics of these fluids and providing more accurate descriptions of their behavior under various flow conditions and applications [5-13].

In polymer industries, fluids range from simple Newtonian liquids to complex non-Newtonian fluids with shear-thinning, shearthickening, or viscoelastic behavior. The EPF model [14] relies on the principles of the kinetic theory of liquids rather than on empirical formulas. This approach involves considering the molecular dynamics and interactions within the fluid, incorporating factors such as molecular structure, activation energy, and transition state theory. Several factors like melt viscosity, shear rate, and residence time, impacting the quality and properties of the final polymer products. The Eyring-Powell fluid model demonstrates notable accuracy and consistency in calculating the fluid time scale across various polymer concentrations [15,16]. Javed et al. [17] employed the Keller box method to numerically investigate the locally similar solution of Evring-Powell fluid. Havat et al. [18] analyzed the flow over a flat surface moving in a parallel free stream of Eyring-Powell fluid. Series solutions of locally similar equations are constructed via homotopy analysis method. Qasim [19] studied the import of Soret and Dufour effect on the Blasius flow over a flat plate subject to convective boundary conditions. Locally similar solutions are computed using shooting method. Farooq et al. [20] performed the entropy production analysis of Eyring-Powell blood-based fluid driven by a stretching surface. Rahimi et al. [21] used the collocation method in the computation arising in the flow of Eyring-Powell fluid over a linearly stretched sheet. Ibrahim and Lamesse [22] examined the magnetohydrodynamic flow of the Eyring-Powell nanofluid under passive control of nanoparticles above a convectively heated stretching surface. Numerical simulations of the coupled locally similar equations are performed using finite element method. Vafai et al. [23] discussed the impact of thermal radiation, Soret and Dufour effects on the flow of electrically conducting Powell-Eyring fluid induced by a stretching sheet. Ambreen et al. [24] discussed the magnetohydrodynamics of Powell-Eyring fluid and heat transfer characteristics by utilizing the Cattaneo-Christov heat flux over a curved stretching surface.

Some attempts have been made to attain self-similar solutions by imposing restrictions on the surface velocity and this is only possible for a particular choice of free stream and surface velocity. Jalil at al. [25] transformed the governing equations into self-similar ordinary differential equations by employing invariant group of transformations. They reported that the resulting equations are self-similar in nature for special type of non-linear free stream velocity and the surface temperature. In the above studies on the boundary layer flows, Eyring -Powell fluid parameter is based on the length scale and containing a spatial coordinate after employing the transformations and the equations are considered as locally similar. Self-similar equations for the Blasius flow of Eyring-Powell fluid are derived by Avramenko et al. [26].

In the articles [17-22], the transformations applied to the governing partial differential equations (PDEs) do not entirely simplify them to ordinary differential equations (ODEs). The stream-wise coordinate remains present in the non-Newtonian fluid parameter. Therefore, considering these equations as ordinary differential equations (ODEs), independent of the stream-wise coordinate, is fundamentally flawed. In fact, under such circumstances, the typical similarity transformations fail to operate effectively, and the

Table 1Transformations and partial derivatives utilized in Eqs. (2)-(5).

$$\begin{aligned} & \text{Transformations:} \begin{cases} \Psi = x\sqrt{s_0\nu}g(\eta,\xi), \xi = \frac{\rho s_0^3 x^2}{c^2\mu}, \eta = y\sqrt{\frac{s_0}{\nu}}, T(\eta,\xi) = \frac{T^* - T_\infty^*}{T_s^* - T_\infty^*}, \\ u^* = s_0x\frac{\partial g}{\partial \eta}, v^* = -\sqrt{s_0\nu}\left\{g(\eta,\xi) + 2\xi\frac{\partial g}{\partial \xi}\right\} \end{cases} \end{aligned}$$
 Partial derivatives utilized in momentum equation
$$\begin{aligned} & \frac{\partial u^*}{\partial x} = s_0\left(\frac{\partial g}{\partial \eta} + 2\xi\frac{\partial^2 g}{\partial \xi\partial \eta}\right) & \frac{\partial T^*}{\partial x} = 2\left(T_s^* - T_\infty^*\right)\xi\frac{\partial T}{\partial \xi} + 2T^*T_0^*x \\ & \frac{\partial u^*}{\partial y} = s_0x\sqrt{\frac{s_0}{\nu}}\frac{\partial^2 g}{\partial \eta^2} & \begin{cases} \frac{\partial T^*}{\partial y} = \left(T_s^* - T_\infty^*\right)\sqrt{\frac{s_0}{\nu}}\frac{\partial T}{\partial \eta} \\ \frac{\partial u^*}{\partial y} = s_0x\sqrt{\frac{s_0}{\nu}}\frac{\partial^2 g}{\partial \eta^2} \end{cases} & \frac{\partial^2 T^*}{\partial y^2} = \left(T_s^* - T_\infty^*\right)\frac{s_0}{\nu}\frac{\partial^2 T}{\partial \eta^2} \end{aligned}$$

treatment of these problems as locally similar leads to significant errors. It is noteworthy to mention that this mistake has been identified by Pantokratoras [27] and now it is being corrected by computation of non-similar solutions [28-36]. In non-similar equations, the dimensionless stream function and temperature display dependence on the stream wise coordinate, alongside their common dependence on the similarity variable [37].

Non-similar equations are the non-linear PDEs. Researchers employed different methodologies to compute the numerical solutions of these equations. Local non similar method (LNS) proposed by Sparrow et al. [38] has been widely employed to tackle these problems. In this procedure, non-similar equations are further transformed into ODEs at different levels of truncations. Afridi et al. [39] observed that the relative percentage error is significantly higher between the 1st and 2nd levels of truncation compared to the 2nd and 3rd levels. Only, few attempts have been made to address the non-similar partial differential equations without converting them into ordinary differential equations. [40-42].

In this article, the magnetohydrodynamic flow of an Eyring–Powell fluid over a linearly stretched surface is investigated in the presence of Joule and viscous dissipation. New transformations are introduced to convert the dimensional PDEs to non-similar dimensionless PDEs. OMD-BSLLM technique [43-45] is implemented to compute the numerical solution of these non-similar equations.

2. Development of the problem

Consideration is given to the steady incompressible dissipative flow of an EPF over a stretching sheet. A two-dimensional model is utilized, employing rectangular Cartesian coordinates $\langle x,y\rangle$, here x and y represent the coordinates parallel and normal to the stretched surface, respectively. Fig. 1 illustrates the physical model along with the coordinate system for this scenario. Additionally, a magnetic field of magnitude H_0 is imposed perpendicular to the stretched surface. The velocity and temperature of the sheet are respectively defined as $u_s^* = s_0 x$ and $T_s^* = T_\infty^* + T_0^* x^2$. The ambient temperature of the fluid is indicated by T_∞^* , whereas, s_0 and T_0^* represent

consideration of viscous dissipation in the energy equation, leading to the formulation of the fundamental equations.

To address this scenario, the relevant balance laws as outlined in literature [16-20] are considered.

$$\frac{\partial u^*}{\partial x} + \frac{\partial v^*}{\partial y} = 0,\tag{1}$$

$$u^{*}\frac{\partial u^{*}}{\partial x} + v^{*}\frac{\partial u^{*}}{\partial y} = \frac{\partial}{\partial y}\left(\nu\frac{\partial u^{*}}{\partial y} + \frac{1}{c\rho\beta}\frac{\partial u^{*}}{\partial y} - \frac{1}{6c^{3}\rho\beta}\left(\frac{\partial u^{*}}{\partial y}\right)^{3}\right) - \frac{\sigma H_{0}^{2}}{\rho}u^{*},\tag{2}$$

$$u^* \frac{\partial T^*}{\partial x} + v^* \frac{\partial T^*}{\partial y} = \frac{k}{\rho c_p} \left(\frac{\partial^2 T^*}{\partial y^2} \right) + \frac{1}{\rho c_p} \left(\sigma H_0^2 u^{*2} + \left(\mu + \frac{1}{c\beta} \right) \left(\frac{\partial u^*}{\partial y} \right)^2 - \frac{1}{6c^3 \beta} \left(\frac{\partial u^*}{\partial y} \right)^4 \right), \tag{3}$$

$$u^* = u_s^* = s_0 x, T^* = T_s^* = T_\infty^* + T_0^* x^2,$$
 at $y = 0$, (4)

The system of PDEs (2) and (3), along with BCs (4) and (5), does not conform to a self-similar form through the typical similarity

 Table 2

 Dimensionless flow parameters with fixed and range of values.

Physical flow Parameters	Symbols with Expressions	Fixed Values	Range of Values
Prandtl Number	$Pr = \frac{c_p \mu}{L}$	2.0	Pr=2.0, 5.0, 7.0, 10.0
Eckert Number	$Ec = \frac{s_0^2}{c_p T_0^*}$	0.5	Ec = 0, 0.2, 0.4, 0.6
Hartmann Number	$H_m^2 = \frac{\sigma B_0^2}{s_0 \rho}$	1.0	$H_m = 0.0, 0.5, 1.0, 1.5$
Fluid Parameter	$\lambda = \frac{1}{\rho \beta \nu c}$	0.5	$\lambda = 1.0, 3.0, 5.0, 8.0$
$\label{lem:point} Dimensionless \ stream-wise \ coordinate \ / \ non-Newtonian \ fluid \ Parameter.$	$\xi = \frac{\rho x^2 s_0^3}{c^2 \mu}$	0.5	$\xi = 0.0, 1.0, 2.0, 3.0$

transformations. i.e. $\left\{ \Psi(\eta) = x \sqrt{s_0 \nu} g(\eta), \eta = y \sqrt{\frac{s_0}{\nu}}, T(\eta) = \frac{T^* - T_\infty^*}{T_s^* - T_\infty^*} \right\}$ and this is because dimensional streamwise coordinate(x) remains

present within the resulting system (more explicitly one of the non-Newtonian parameters is not free from x), leading to the conclusion that self-similar solution of the governing system does not exist. Consequently, adjustments to these transformations are necessary to incorporate the explicit dependence of Ψ and T on dimensionless streamwise coordinate ξ in the following manner.

$$\left\{\Psi = x\sqrt{s_0\nu} g(\eta, \xi), \xi = \frac{\rho s_0^3 x^2}{c^2 \mu}, \eta = y\sqrt{\frac{s_0}{\nu}}, T(\eta, \xi) = \frac{T^* - T_{\infty}^*}{T_{\infty}^* - T_{\infty}^*}\right\}.$$
 (6)

To achieve dimensionless form of a system of PDEs, various mathematical transformations and manipulations are applied to the momentum and energy equations along with their respective boundary conditions, as outlined in Table 1.

Accordingly, Eqs. (2)–(5) undergo these transformations and resulting in the subsequent system.

$$(1+\lambda)\frac{\partial^{3}g}{\partial\eta^{3}} - \frac{\lambda\xi}{2}\left(\frac{\partial^{2}g}{\partial\eta^{2}}\right)^{2}\frac{\partial^{3}g}{\partial\eta^{3}} - H_{m}^{2}\frac{\partial g}{\partial\eta} + g\frac{\partial^{2}g}{\partial\eta^{2}} - \left(\frac{\partial g}{\partial\eta}\right)^{2} + \begin{cases} 2\xi\frac{\partial^{2}g}{\partial\eta^{2}}\frac{\partial g}{\partial\xi} - 2\xi\frac{\partial g}{\partial\eta}\frac{\partial^{2}g}{\partial\xi\partial\eta} = 0 \end{cases}$$

$$(7)$$

$$\frac{1}{\Pr} \frac{\partial^{2} T}{\partial \eta^{2}} + g \frac{\partial T}{\partial \eta} - 2T \frac{\partial g}{\partial \eta} + H_{m}^{2} E c \left(\frac{\partial g}{\partial \eta}\right)^{2} + 2\xi \frac{\partial T}{\partial \eta} \frac{\partial g}{\partial \xi} - 2\xi \frac{\partial g}{\partial \eta} \frac{\partial T}{\partial \xi} + \left. \left\{ \frac{\partial^{2} g}{\partial \eta^{2}} \right\}^{2} \left[(1+\lambda) - \frac{1}{6} \xi \lambda \left(\frac{\partial^{2} g}{\partial \eta^{2}}\right)^{2} \right] = 0$$
(8)

$$\frac{\partial g(\eta, \xi)}{\partial \eta} = 1$$

$$g(\eta, \xi) + 2\xi \frac{\partial g(\eta, \xi)}{\partial \eta} = 0$$

$$T(\eta, \xi) = 1$$
(9)

$$\frac{\partial g(\eta,\xi)}{\partial \eta} \rightarrow 0 \left. \right\}_{\eta \to \infty}$$

$$T(\eta,\xi) \rightarrow 0 \right\}_{\eta \to \infty}$$
(10)

The dimensionless parameters appearing in the above system are defined in Table 2. The non-dimensional version of skin friction coefficient $[C_{fx}]$ and Nusselt number $[N_{ux}]$ are given below

$$\sqrt{\operatorname{Re}_{x}}C_{fx} = (1+\lambda)\frac{\partial^{2}g(\eta,\xi)}{\partial\eta^{2}} - \frac{1}{6}\lambda\xi\left(\frac{\partial^{2}g(\eta,\xi)}{\partial\eta^{2}}\right)^{3} \\
\frac{N_{ux}}{\sqrt{\operatorname{Re}_{x}}} = -\frac{\partial T(\eta,\xi)}{\partial\eta}$$
(11)

3. Solution methodology

This section delves into the detailed implementation of OMD-BSLLM on the non-linear system of Eqs. (7)–(10). It is worth mentioning that in the present study, the non-Newtonian fluid parameter ξ is playing the role of the time variable in MD-BSLLM [46] and OMD-BSLLM [43-45]. The numerical approach consists of five fundamental steps. First, linearization is achieved through the local

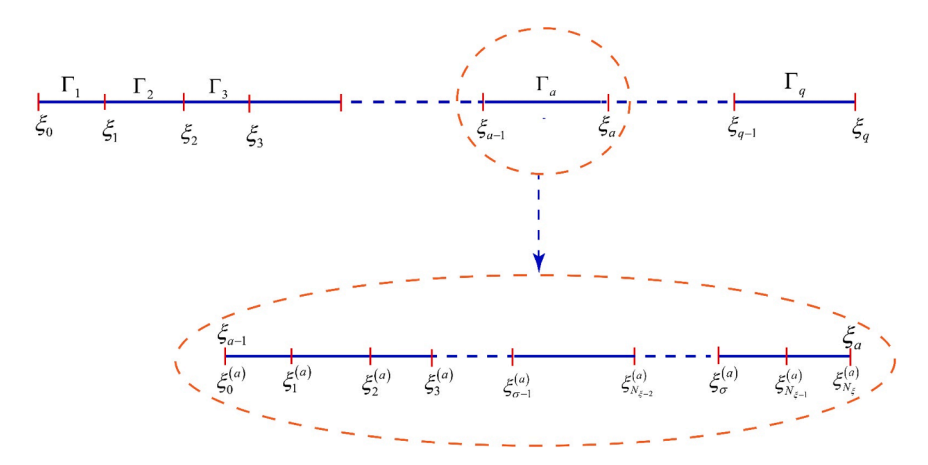


Fig. 2. Decomposing the ξ – domain into non-overlapping multiple sub-domains.

linearization method (LLM). Next, the space computational domains in ξ – and η – directions are divided into multiple intervals that are non-overlapping and overlapping, respectively. Following that, the unknown functions and their continuous derivatives are approximated using bivariate Lagrange interpolating polynomials. Lastly, the linearized iterative scheme is solved using the spectral collocation method (SCM), employing Chebyshev-Gauss-Lobatto (CGL) points as collocation points. Applying the LLM algorithm to simplify the transport Eqs. (7) and (8) results in the following system of linear equations:

$$\beta_{0,r} \frac{\partial^{3} g_{r+1}}{\partial \eta^{3}} + \beta_{1,r} \frac{\partial^{2} g_{r+1}}{\partial \eta^{2}} + \beta_{2,r} \frac{\partial g_{r+1}}{\partial \eta} + \beta_{3,r} g_{r+1} + \beta_{4,r} \frac{\partial}{\partial \eta} \left(\frac{\partial g_{r+1}}{\partial \xi} \right) + \beta_{5,r} \left(\frac{\partial g_{r+1}}{\partial \xi} \right) = \beta_{6,r},$$

$$(12)$$

$$\gamma_{0,r} \frac{\partial^2 T_{r+1}}{\partial \eta^2} + \gamma_{1,r} \frac{\partial T_{r+1}}{\partial \eta} + \gamma_{2,r} T_{r+1} + \gamma_{3,r} \left(\frac{\partial T_{r+1}}{\partial \xi} \right) = \gamma_{4,r},\tag{13}$$

where the variable coefficients, which are assumed to be derived from the preceding iteration (r), are defined as

$$\beta_{0,r} = (1+\lambda) - \frac{1}{2}\lambda\xi \left(\frac{\partial^2 g_r}{\partial \eta^2}\right)^2, \beta_{1,r} = g_r - \lambda\xi \frac{\partial^2 g_r}{\partial \eta^2} \frac{\partial^3 g_r}{\partial \eta^3} + 2\xi \frac{\partial g_r}{\partial \xi},$$

$$\beta_{2,r} = -H_m^2 - 2\frac{\partial g_r}{\partial \eta} - 2\xi \frac{\partial}{\partial \eta} \left(\frac{\partial g_r}{\partial \xi}\right), \beta_{3,r} = \frac{\partial^2 g_r}{\partial \eta^2}, \beta_{4,r} = -2\xi \frac{\partial g_r}{\partial \xi},$$

$$\beta_{5,r} = 2\xi \frac{\partial^2 g_r}{\partial \eta^2}, \beta_{6,r} = g_r \frac{\partial^2 g_r}{\partial \eta^2} - \left(\frac{\partial g_r}{\partial \eta}\right)^2 - 2\xi \frac{\partial g_r}{\partial \eta} \frac{\partial}{\partial \eta} \left(\frac{\partial g_r}{\partial \xi}\right) + 2\xi \frac{\partial^2 g_r}{\partial \eta^2} \frac{\partial g_r}{\partial \xi}$$

$$\lambda\xi \frac{\partial^3 g_r}{\partial \eta^3} \left(\frac{\partial^2 g_r}{\partial \eta^2}\right)^2, \gamma_{0,r} = \frac{1}{\Pr}, \gamma_{1,r} = g_r + 2\xi \frac{\partial g_r}{\partial \xi}, \gamma_{2,r} = -2\frac{\partial g_r}{\partial \eta}, \gamma_{3,r} = -2\xi \frac{\partial g_r}{\partial \eta},$$

$$\gamma_{4,r} = -H_m^2 Ec \left(\frac{\partial g_r}{\partial \eta}\right)^2 - Ec \left(\frac{\partial^2 g_r}{\partial \eta^2}\right)^2 \left((1+\lambda) - \frac{1}{6}\lambda\xi \left(\frac{\partial^2 g_r}{\partial \eta^2}\right)^2\right),$$

It is worth noting that the superscript (r+1) represents the current iteration level. Following this, it is assumed that ξ belongs to the set Γ , where $\Gamma = [0, \xi_F]$ represents the domain of approximation in the ξ – direction. Subsequently, Γ is divided into q equal and small non-overlapping sub-intervals, which are designated as follows:

$$\Gamma_a = [\xi_{a-1}, \xi_a], \xi_{a-1} < \xi_a, 0 = \xi_0 < \xi_1 < \dots < \xi_{q-1} < \xi_q = \xi_F, a = 1, 2, 3, 4, \dots, q.$$

$$\tag{15}$$

The problem is addressed within each sub-interval to ensure compliance with the pertinent boundary conditions. The solution attained by solving the transport equations at $\xi=0$ serves as an initial condition within the 1st first sub-interval Γ_1 . Subsequently, for the next sub-intervals $\Gamma_a(a=2,3,4,5,...,q)$, the solution obtained at the final grid point of the preceding sub-interval Γ_{a-1} is utilized as an initial condition for the succeeding sub-interval Γ_a . Fig. 2 illustrates the decomposition of the computational domain in the ξ – direction into qsub-intervals, where $\xi_w^{(a)}(\varpi=0,1,2,3,...,N_\xi,a=1,2,3,4,...,q)$ represents $(N_\xi+1)$ C-G-L collocation grid points within every sub-interval. To apply the SCM method inside the range [-1,1], we utilize the subsequent linear transformation:

$$\xi = \frac{1}{2}(\xi_a - \xi_{a-1})\hat{\xi} + \frac{1}{2}(\xi_a - \xi_{a-1}),\tag{16}$$

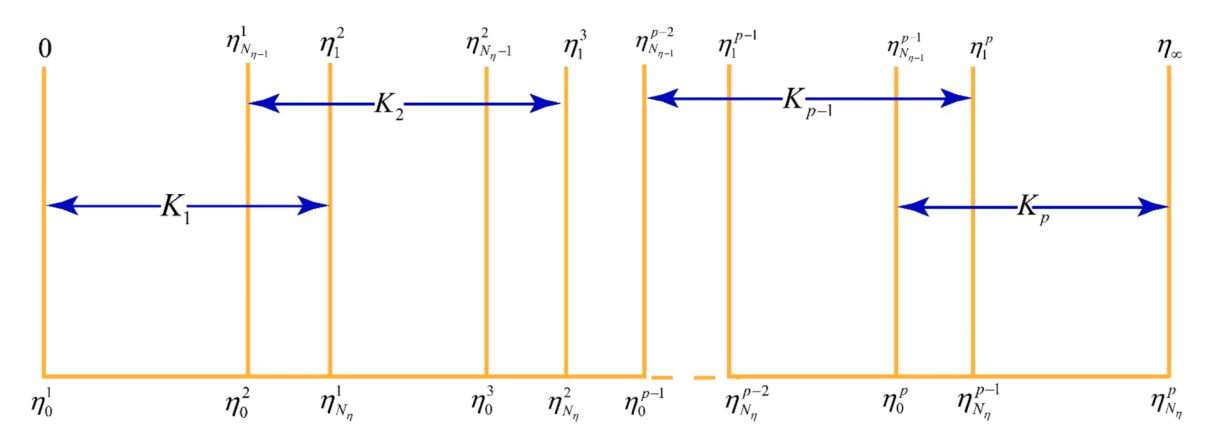


Fig. 3. Decomposing the η – domain into overlapping multiple sub-domains.

to convert the physical variable $\xi \in [\xi_{a-1}, \xi_a]$ in the a^{th} sub-interval into the collocation variable $\hat{\xi} \in [-1,1]$. The domain inside every sub-interval is then discretized via $(N_{\xi}+1)$ CGL collocation points, which are defined in [40-42]

$$\left\{\widehat{\xi}_{j}\right\}_{j=0}^{N_{\xi}} = \cos\left(\frac{j\pi}{N_{\varepsilon}}\right). \tag{17}$$

Conversely, the physical domain in the η direction is first truncated into the domain $K = [0, \eta_{\infty}]$, where η_{∞} is selected to adequately fulfill the far-field boundary conditions. Then the domain K is partitioned into p overlapping sub-intervals, denoted as follows:

$$K_b = [\eta_0^b, \eta_{N_c}^b], b = 1, 2, 3, ..., p.$$
(18)

Every sub-interval in direction of η shares a uniform length $L = \frac{\eta_{\infty}}{p + \frac{1}{2}(1-p)\left(1-\cos\left(\frac{\pi}{N_{\eta}}\right)\right)}$, and every sub-domain employs the equal

number of

CGL collocation points $(N_{\eta} + 1)$. Fig. 3 depicts the division of the η – domain into poverlapping sub-intervals. Here, the final two grid points of interval K_b align with the initial two grid points of the subsequent sub-interval, denoted by K_{b+1} For detailed formulations describing the lengths of sub-interval L, the reader is advised to consult the publications of [46,47].

Analogous to the conversion of the ξ – domain, the following linear mapping

$$\widehat{\eta} = \frac{2}{\eta_{N_{\eta}}^{b} - \eta_{0}^{b}} \eta - \frac{\eta_{N_{\eta}}^{b} + \eta_{0}^{b}}{\eta_{N_{\eta}}^{b} - \eta_{0}^{b}},\tag{19}$$

are utilized in the transformation of the physical variable $\eta \in \left[\eta_0^b, \eta_{N_\eta}^b\right]$ onto the collocation variable $\widehat{\eta} \in [-1, 1]$ The collocation points in the K_a interval is given by

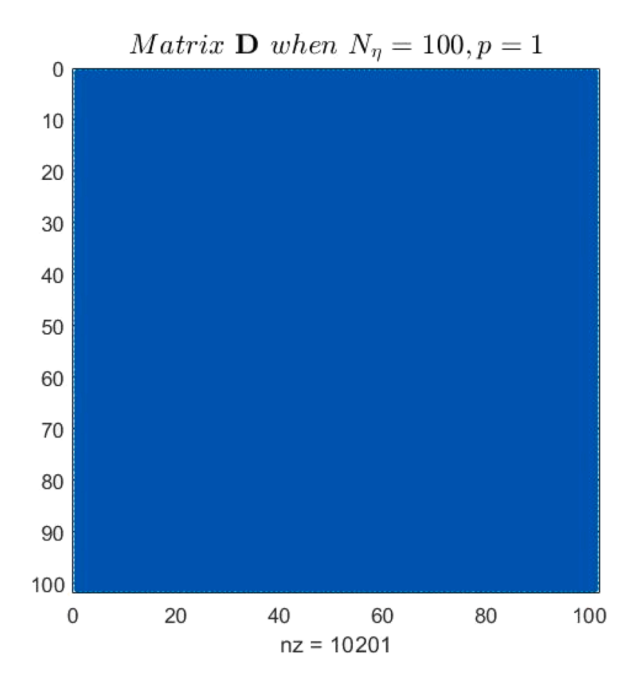
$$\{\widehat{\eta}_i\}_{i=0}^{N_{\eta}} = \cos\left(\frac{i\pi}{N_{\eta}}\right). \tag{20}$$

To differentiate the solutions across different sub-domains in the ξ – direction, we utilize the notations $g^{(a)}(\eta, \xi)$ and $T^{(a)}(\eta, \xi)$, where a=1,2,3,...,q, to represent the solutions within the ath sub-interval. It is important to highlight that equations are solved separately within every sub-interval along the ξ – direction, whereas solutions are simultaneously evaluated across overlapping sub-intervals along the η – direction. Therefore, the linearized LLM scheme evolves to

$$\beta_{0,r} \frac{\partial^{3} \mathbf{g}_{r+1}^{(a)}}{\partial \eta^{3}} + \beta_{1,r} \frac{\partial^{2} \mathbf{g}_{r+1}^{(a)}}{\partial \eta^{2}} + \beta_{2,r} \frac{\partial \mathbf{g}_{r+1}^{(a)}}{\partial \eta} + \beta_{3,r} \mathbf{g}_{r+1}^{(a)} + \beta_{4,r} \frac{\partial}{\partial \eta} \left(\frac{\partial \mathbf{g}_{r+1}^{(a)}}{\partial \xi} \right) + \beta_{5,r} \left(\frac{\partial \mathbf{g}_{r+1}^{(a)}}{\partial \xi} \right) = \beta_{6,r}, \tag{21}$$

$$\gamma_{0,r} \frac{\partial^2 T_{r+1}^{(a)}}{\partial m^2} + \gamma_{1,r} \frac{\partial T_{r+1}^{(a)}}{\partial m} + \gamma_{2,r} T_{r+1}^{(a)} + \gamma_{3,r} \left(\frac{\partial T_{r+1}^{(a)}}{\partial \mathcal{E}} \right) = \gamma_{4,r}. \tag{22}$$

In the initial interval $[\xi_0,\xi_1]$, the solutions $g^{(1)}(\eta,\xi)$ and $T^{(1)}(\eta,\xi)$ are determined under the initial conditions $g^{(1)}(0,\xi)$ and $T^{(1)}(0,\xi)$. Subsequently, in the remaining sub-intervals $\Gamma_a(a=2,3,4,5,...,q)$, the continuity conditions are enforced in the execution of the OMD-BSLLM scheme across the interval $[\xi_{a-1},\xi_a]$. This process is repeated to generate the series of solutions $g^{(a)}(\eta,\xi)$ and $T^{(a)}(\eta,\xi)$, where a=1,2,3,...,p. During the solution process, the specified type of bivariate Lagrange interpolation polynomial that can be expressed in the following manner:



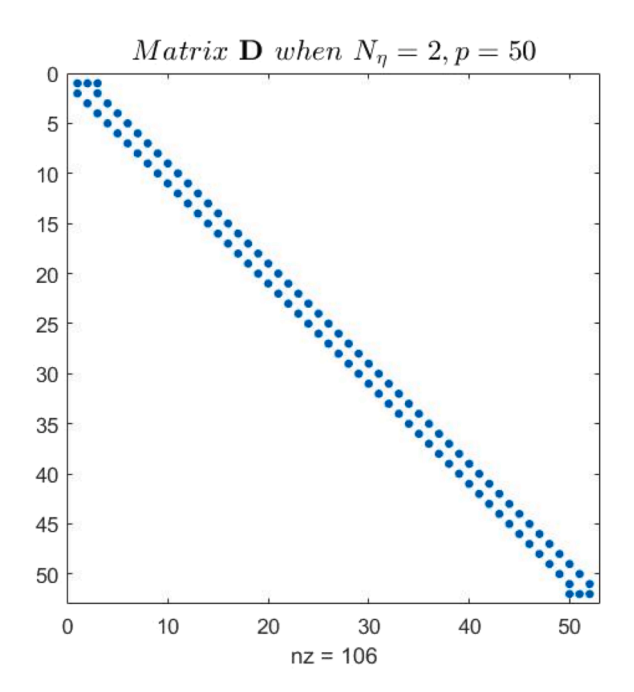


Fig. 4. Sparsity pattern of the matrix D for the OMD-BSLLM and MD-BSLLM schemes.

$$g^{(a)}(\eta,\xi) \approx G^{(a)}(\eta,\xi) = \sum_{k=0}^{N_{\eta}} \sum_{l=0}^{N_{\xi}} G^{(a)}(\eta_k,\xi_l) L_k(\eta) L_l(\xi), \tag{23}$$

is employed in the approximation of the solution of $g(\eta, \xi)$ within every sub-interval in ξ – direction. The estimation of the first-order spatial derivative matrix w.r.t the variable η is performed via $(\widehat{\eta}_i, \widehat{\xi}_j)$, for $j = 0, 1, 2, 3, ..., N_{\xi}$, within in each b^{th} sub-interval as follows:

$$\frac{\partial g^{(a)}}{\partial \eta} \left(\widehat{\eta}_i, \widehat{\xi}_j \right) = \sum_{k=0}^{N_q} \sum_{l=0}^{N_{\xi}} G^{(a)}(\eta_k, \xi_l) L'_k(\widehat{\eta}) L_l(\widehat{\xi}) = \sum_{k=0}^{N_q} G^{(a)} \left(\eta_k, \xi_j \right) L'_k(\widehat{\eta}) = \mathbf{D} \mathbf{G}_j^{(a)}, \tag{24}$$

where $D = \frac{2}{L}\overline{D}$, and \overline{D} represents the fundamental first-order Chebyshev differential matrix (CDM) with dimensions $(N_{\eta} + 1) \times (N_{\eta} + 1)$ [47-49]. On the other hand, the matrix-vector denoted by $G_i^{(a)}$ with matrix size $(N_{\eta} + 1) \times 1$ is given by

$$\mathbf{G}_{i}^{(a)} = \left[g^{(a)}(\eta_{0}^{(b)}, \xi_{i}), g^{(a)}(\eta_{1}^{(b)}, \xi_{i}), ..., g^{(a)}(\eta_{N}^{(b)}, \xi_{i}) \right]^{t}, b = 1, 2, 3, ..., p,$$

$$(25)$$

where t denotes the transpose operation on matrices. The n^{th} order derivative matrices concerning the spatial variable η can be obtained through matrix multiplication as

$$\frac{\partial^n g^{(a)}}{\partial \eta^n} \left(\widehat{\eta}_i, \widehat{\xi}_j \right) = \mathbf{D}^n \mathbf{G}_j^{(a)}. \tag{26}$$

Subsequently, the estimation of the first order derivative matrix w.r.t ξ is carried out via $(\hat{\eta}_i, \hat{\xi}_j)$, for $j = 0, 1, 2, 3, ..., \xi$, within in each a^{th} sub-interval as follows:

$$\frac{\partial g^{(a)}}{\partial \xi} (\widehat{\eta}_i, \widehat{\xi}_j) = \left(\frac{2}{\xi_a - \xi_{a-1}}\right) \sum_{l=0}^{N_{\xi}} \overline{d}_{j,l} \overline{G}_l^{(a)} = \sum_{l=0}^{N_{\xi}} d_{j,l} \overline{G}_l^{(a)}, \tag{27}$$

where $d_{j,l} = \frac{2}{\bar{\xi}_a - \bar{\xi}_{a-1}} \overline{d}_{j,l} (j,l=0,1,2,3,4,...,N_{\xi})$, and the matrix $d_{j,l}$ represents the fundamental first-order CDM with dimensions $(N_{\xi}+1)$ × $(N_{\xi}+1)$ [47-49]. The updated matrix-vector $\overline{G}_i^{(a)}$ of size $(M+1) \times 1$ takes the form

$$\overline{\mathbf{G}}_{i}^{(a)} = \left[g^{(a)}(\eta_{0}, \xi_{i}), g^{(a)}(\eta_{1}, \xi_{i}), ..., g^{(a)}(\eta_{M}, \xi_{i}) \right]^{t}, a = 1, 2, 3, ..., q,$$
(28)

where $M = N_{\eta} + (N_{\eta} + 1) \times (p - 1)$ represents all collocation points used across the entire domain in the η direction. The other unknown function $T(\eta, \xi)$ and the derivative matrices corresponding to it are approximated in the same way. In the overlapping multidomain approach, the spatial Chebyshev differential matrix D w.r.t the variable η has the matrix size(M+1) \times (M+1). Because of the overlapping scheme, the 1^{st} and last two grid points in the $(b+1)^{th}$ and b^{th} sub-intervals coincide, being treated as one grid point. As a result, Consequently, the rows associated with duplicated mesh points are excluded while building the Chebyshev derivative matrix D, following the structure outlined in [43-47]. In the structure, the non-zero elements are represented by colored pixels and the zero elements are left blank. To visualize the structure of the matrix D, the 'spy' function is used in MATLAB to plot the sparsity pattern of the Chebyshev differentiation matrix **D** as seen in Fig. 4. From the figure, it is noted that the differentiation matrix resulting from the overlapping grid-based spectral collocation method is less dense or sparse as it is characterized by many zero elements. Thus, this Chebyshev derivative matrix leads to significant computational savings in operations such as matrix-vector multiplication and solving linear systems. This is because operations involving zero elements can often be skipped, minimizing the number of arithmetic operations required. This sparse matrix will also require less memory to store when compared to dense matrices from the MD-BSLLM approach which stores every element explicitly. Sparse matrices play a crucial role in applications where memory is limited such as in numerical modeling. The sparsity pattern can affect various properties of a matrix, such as its condition number. Thus, understanding the sparsity pattern can help in analyzing the condition number and designing appropriate numerical methods. More details on condition numbers will be discussed in the results and discussion section.

The utilization of SCM involves substituting continuous derivatives with discrete ones and incorporating initial conditions. Thus, we have the following matrix equations

$$(\beta_{0,r}\mathbf{D}^{3} + \beta_{1,r}\mathbf{D}^{2} + \beta_{2,r}\mathbf{D}^{3} + \beta_{3,r})\overline{\mathbf{G}}_{i}^{(a)} + \beta_{4,r}\sum_{i=0}^{N_{\xi-1}}d_{i,j}\mathbf{D}\overline{\mathbf{G}}_{j,r+1}^{(a)} + \beta_{5,r}\sum_{i=0}^{N_{\xi-1}}d_{i,j}\mathbf{D}\overline{\mathbf{G}}_{j,r+1}^{(a)} = \mathbf{R}_{1,r}^{(a)},$$
(29)

$$\left(\gamma_{0,r} D^2 + \gamma_{1,r} D + \gamma_{2,r}\right) \overline{T}_i^{(a)} + \gamma_{3,r} \sum_{j=0}^{N_{\ell-1}} d_{i,j} \overline{T}_{j,r+1}^{(a)} = \mathbf{R}_{2,r}^{(a)}, \tag{30}$$

where the vectors \overline{G} and \overline{T} are of size (M+1), and

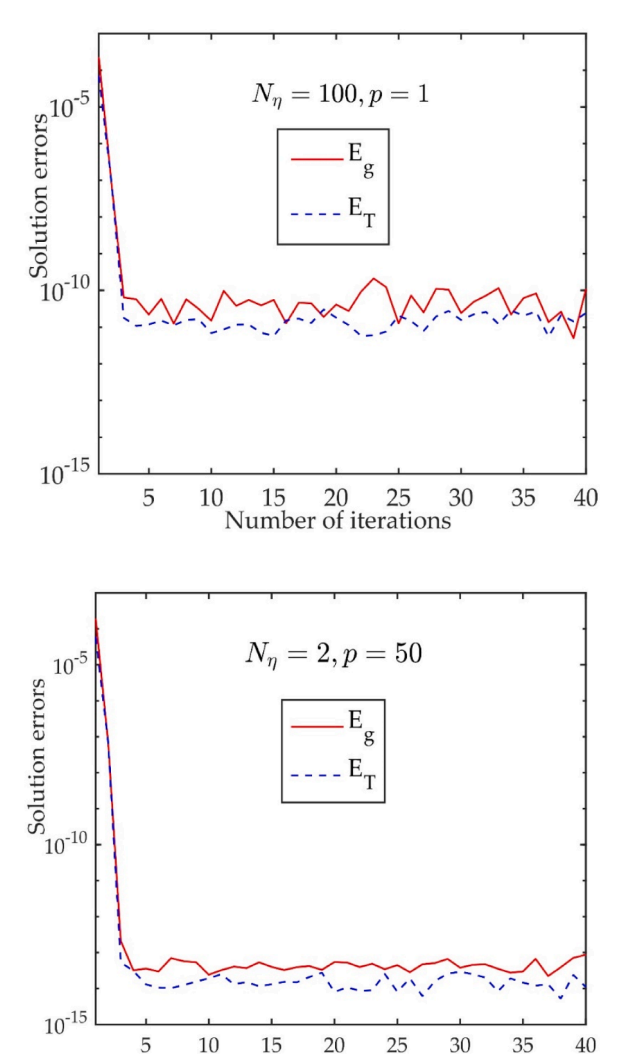


Fig. 5. Convergence error for the OMD-BSLLM and MD-BSLLM schemes.

$$\left.\begin{array}{l}
\mathbf{R}_{1,r}^{(a)} = \boldsymbol{\beta}_{6,r} - \boldsymbol{\beta}_{4,r} d_{i,N_{\xi}} \mathbf{D} \overline{\mathbf{G}}_{N_{\xi}}^{(a)} - \boldsymbol{\beta}_{5,r} d_{i,N_{\xi}} \overline{\mathbf{G}}_{N_{\xi}}^{(a)} \\
\mathbf{R}_{2,r}^{(a)} = \boldsymbol{\gamma}_{4,r} - \boldsymbol{\gamma}_{3,r} d_{i,N_{\xi}} \overline{\mathbf{T}}_{N_{\xi}}^{(a)}
\end{array}\right\}.$$
(31)

Number of iterations

Similarly, the corresponding boundary conditions are also evaluated at the collocation points. Eq. (28) can be expressed in matrix form using the square matrix with a size of $N_{\varepsilon}(M+1) \times N_{\varepsilon}(M+1)$:

$$\begin{bmatrix} \mathbf{A}_{0,0} & \mathbf{A}_{0,1} & \mathbf{A}_{0,2} & \cdots & \mathbf{A}_{0,N_{\xi}-1} \\ \mathbf{A}_{1,0} & \mathbf{A}_{1,1} & \mathbf{A}_{1,2} & \cdots & \mathbf{A}_{1,N_{\xi}-1} \\ \vdots & \vdots & \ddots & \cdots & \vdots \\ \mathbf{A}_{N_{\xi}-1,0} & \mathbf{A}_{N_{\xi}-1,0} & \mathbf{A}_{N_{\xi}-1,0} & \cdots & \mathbf{A}_{N_{\xi}-1,N_{\xi}-1} \end{bmatrix} \begin{bmatrix} \overline{\mathbf{G}}_{0}^{(a)} \\ \overline{\mathbf{G}}_{0}^{(a)} \\ \vdots \\ \overline{\mathbf{G}}_{N_{\xi}-1}^{(a)} \end{bmatrix} = \begin{bmatrix} \mathbf{R}_{1,0}^{(a)} \\ \mathbf{R}_{1,1}^{(a)} \\ \vdots \\ \mathbf{R}_{1,N_{\xi}-1}^{(a)} \end{bmatrix},$$

$$(32)$$

where $\mathbf{A}_{i,i} = \boldsymbol{\beta}_{0,r} \mathbf{D}^3 + \boldsymbol{\beta}_{1,r} \mathbf{D}^2 + \boldsymbol{\beta}_{2,r} \mathbf{D} + \boldsymbol{\beta}_{3,r} \mathbf{I} + \boldsymbol{\beta}_{4,r} d_{i,i} \mathbf{D} + \boldsymbol{\beta}_{5,r} d_{i,i} \mathbf{I}$ when i = j, $\mathbf{A}_{i,i} = \boldsymbol{\beta}_{4,r} d_{i,j} \mathbf{D} + \boldsymbol{\beta}_{5,r} d_{i,j} \mathbf{I}$ when $i \neq j$ and the identity matrix I has dimension $(M+1) \times (M+1)$. The other matrix Eq. (29) can be can be represented as a matrix system analogous to (31). Boundary constraints are integrated into the leading diagonal sub-blocks of the matrix systems, creating a new set of linear algebraic equations. These equations are solved iteratively, starting with initial approximations $g_0(\eta) = 1 - e^{-\eta}$ and $T_0(\eta) = e^{-\eta}$, to obtain the desired solutions.

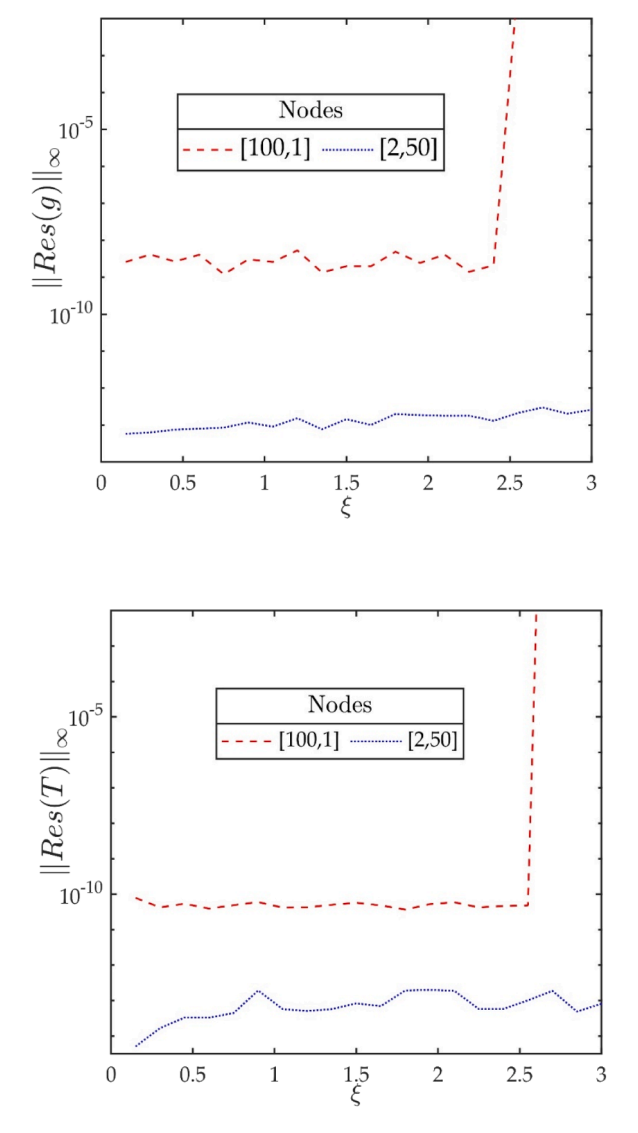


Fig. 6. Residual error graphs for the OMD-BSLLM and MD-BSLLM schemes.

 Table 3

 Residual error values and condition numbers for OMD-BLLM and MD-BLLM.

p	N_{η}	$\parallel \operatorname{Res}(g) \parallel_{\infty}$	$\parallel \operatorname{Res}(T) \parallel_{\infty}$	Cond (A)	Cond (B)	CPU Time (s)
1	100	1.75581e-09	3.96368e-11	1.19692e+09	9.35557e+05	3.02010
2	50	9.99671e-10	7.14506e-12	1.27780e+08	2.67797e+05	2.38297
4	25	1.33251e-10	3.64265e-12	1.45653e+07	6.85595e+04	2.13766
5	20	6.74823e-11	2.76306e-13	7.31624e+06	4.55779e+04	2.11581
10	10	1.14315e-11	2.29286e-13	8.68307e+05	1.63562e+04	1.94834
20	5	2.07924e-12	1.30920e-13	9.91696e+04	9.71883e+03	1.31999
25	4	1.29083e-12	1.03423e-13	7.38454e+04	8.82872e+03	1.17933
50	2	1.58441e-13	1.11774e-13	1.40252e + 04	6.23908e+03	0.59942

4. Results and discussion

Numerical outcomes achieved through OMD-BSLLM are presented in this section of the study. The numerical findings about the flow characteristics, heat transfer, Nusselt number and skin friction coefficient for different key physical parameters are portrayed in figures and tables. By conducting simulations, we have adjusted the parametric values related to the physical flow parameters, as outlined in Table 2. These parameters remain constant or vary according to Table 2 unless explicitly stated otherwise in the

Table 4 Numerical values of $\sqrt{\text{Re}_x} C_{fx}$ against various combinations of flow parameters when Pr=2 and Ec=0.5.

λ	H_m	ξ	$\left(\operatorname{Re}_{x}^{0.5}C_{f_{x}}\right)$
1			-1.9753439
3	1.0	0.5	-2.8026410
5			-3.4412860
8			-4.2250578
	0.0		-1.2170156
0.5	0.5	0.5	-1.3590074
	1.0		-1.7131748
	1.5		-2.1714952
		0.5	-1.7131748
0.5	1.0	1.0	-1.6924797
		2.0	-1.6415499
		3.0	-0.3210619

Table 5Numerical values of $\frac{N_{ux}}{\sqrt{Re_x}}$ against various combinations of flow parameters

	γ ιτέχ				
λ	H_m	ξ	Pr	Ec	$\frac{N_{ux}}{\sqrt{\mathrm{Re}_x}}$
1					1.1454572
3	1.0	0.5	2.0	0.5	1.0799856
5					1.0329824
8					0.9827384
	0.0				1.7358300
0.5	0.5	0.5	2.0	0.5	1.5770014
	1.0				1.1638882
	2.0				0.5989936
1		0.5			1.1638882
3	1.0	1.0	2.0	0.5	1.1605875
5		2.0			1.1511849
8		3.0			1.1428500
1			2.0		1.1638882
3	1.0	0.5	5.0	0.5	1.7182215
5			7.0		1.9608388
8			10		2.2466164
1				0.0	1.9526842
3	1.0	0.5	2.0	0.2	1.6371658
5				0.4	1.3216474
8				0.6	1.0061291

accompanying figures and tables.

The changes in solution errors for the numerical computation of $g(\eta,\xi)$ and $T(\eta,\xi)$ against the iterations are depicted in Fig. 5 for both MD-BSLLM [50] (without overlapping) and OMD-BSLLM schemes. The consistent decrease in solution-based error infinity norms as the number of iterations escalate signifies that the numerical scheme is converging. Complete convergence is achieved when the convergence plots begin to level off or stabilize. As shown in Fig. 5, full convergence occurs after roughly five iterations for all solutions, with solution errors approaching 10^{-11} for the MD-BSLLM and 10^{-14} for OMD-BSLLM algorithm. The small errors associated with the OMD-BSLLM algorithm confirms its superior accuracy.

From Fig. 6, the residual error infinity norms of $g(\eta,\xi)$ and $T(\eta,\xi)$ are graphed are graphed against the dimensionless streamwise coordinate (non-Newtonian fluid parameter) ξ . It is evident that the residual errors are lesser in the OMD-BSLLM compared to the MD-BSLLM, indicating that the overlapping grid-based SCM offers higher accuracy than the MD-BSLLM. Further, it is also noted that residual errors are almost uniform across the non-Newtonian fluid parameter ξ in the OMD-BSLLM scheme and these errors approximate the true solution to about 10^{-13} throughout the ξ – direction. This observation confirms that even for high values of ξ , the OMD-BSLLM scheme produces acceptable errors that ensures reasonably superior accuracy for practical use. This is an advantage of the OMD-BSLLM over the MD-BSLLM whose accuracy deteriorates rapidly when ξ becomes large. The deterioration in the accuracy of the MD-BSLLM is caused by factors such as round-off errors and stability issues. This observation suggests that SCM with overlapping grids effectively generates superior accurate and stable results, even when dealing with large parameter values.

Table 3 illustrate that the small residual errors correspond to the OMD-BSLLM scheme, which basically justifies the superior accuracy of the overlapping grid-based spectral collocation scheme. Also, the coefficient matrices resulting through the implementation of overlapping grid idea are clearly associated with low condition numbers, which indicate that these matrices are well-conditioned and numerically stable. Since these coefficient matrices are well-conditioned, solving the linear systems or computing the inverses is

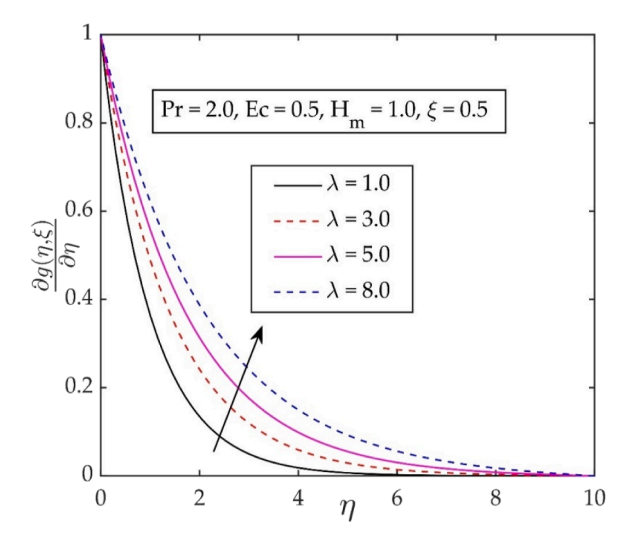


Fig. 7. Impact of fluid parameter λ on the velocity distribution.

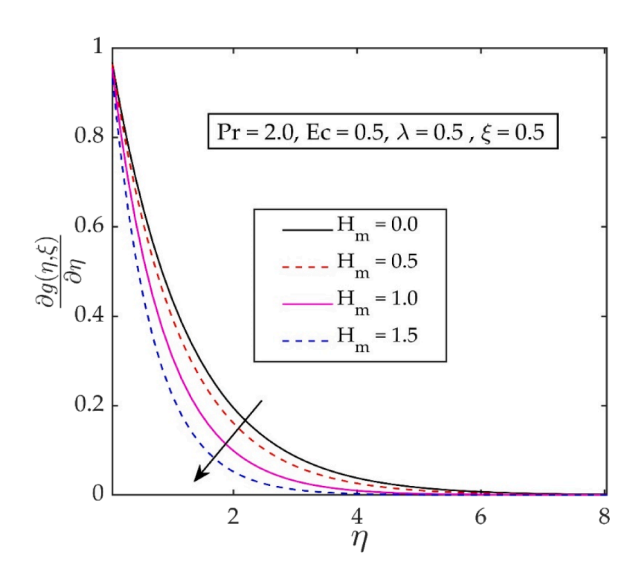


Fig. 8. Impact of Hartman number H_m on the velocity distribution.

less sensitive to errors. Actually, inverting well-conditioned matrices is a stable operation and the inverse of such matrices can be computed accurately. It is also seen that the well-conditioned matrices contribute to less computational time since numerical algorithms converge faster and are more stable when applied to well-conditioned matrices. This stability ensures that the algorithm does not amplify errors during computation, leading to faster, accurate and more reliable results. The well-conditioned nature of the coefficient matrices makes the overlapping grid-based spectral collocation scheme to be computationally efficient, more accurate, and it is less likely to be derailed by instabilities. These properties can be remarkably improved by maximizing the number of overlapping sub-intervals used while minimizing the number of collocation points per sub-interval.

Tables 4 and 5 illustrate the impact of physical parameters on the significant engineering quantities Table 3 validates that the decrease in surface drag force is associated with an increase in fluid parameter λ and Hartmann number H_m , while it is enhanced with dimensionless stream-wise coordinates ξ . According to Table 5, the enhancement in the rate of heat transfer at the surface is observed with an increase in Pr, but is suppressed by the growth of H_m , λ , ξ , and Ec. Additionally, these values are documented to establish benchmark values for potential research endeavors in this field.

The findings regarding fluid parameter λ impact on the velocity profile $g_{\eta}(\eta,\xi)$ are depicted in Fig. 7. The increase in velocity profile is noted as the fluid parameter increases. In physical terms, the fluid parameter λ has an inverse relationship with the fluid's viscosity. When the fluid parameter increases, it implies a decline in the fluid's viscosity, which in turn reduces the internal resistance. As a consequence, the individual layers of the fluid can move more freely, leading to a noticeable increase in velocity profile. Fig. 8 shows a visual illustration of how the Hartman number on velocity profile. The outcomes indicates that the velocity curves decline with

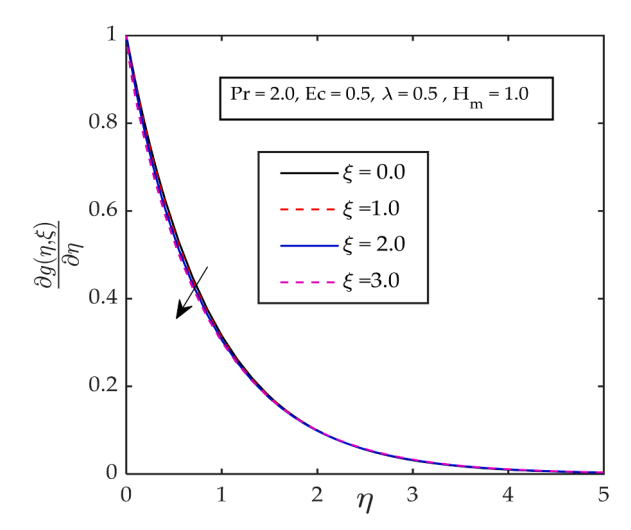


Fig. 9. Impact of dimensionless stream-wise coordinate ξ on the velocity distribution.

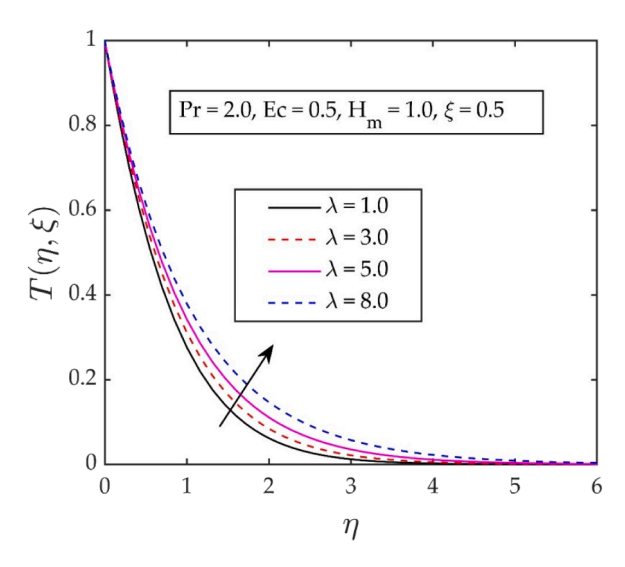


Fig. 10. Impact of fluid parameter λ on the temperature distribution.

incrementing the inputs of Hartman number. The reasoning behind this decline velocity profile is, when the magnetic field applied is intensified (increasing Hartman number), the Lorentz force, representing the force arising from the interplay between the magnetic field and the fluid, exerts its influence on the fluid. This force, perpendicular to both the magnetic field and the fluid velocity, generates a resistance force against the direction of flow. As the Hartman number grows, this force escalates, consequently resulting in a reduction in fluid velocity. In Fig. 9, the prediction of the velocity profile $g_{\eta}(\eta, \xi)$ is presented in relation to the dimensionless variable η for the dimensionless stream-wise coordinate ξ . The graphical representation illustrates a slight decrease in the velocity profile as the dimensionless stream-wise coordinate increases.

Fig. 10 displays how the increment in the fluid parameter λ affects the heat transfer mechanism. The findings disclose that the temperature curves and temperature boundary layer improve by incrementing the inputs of fluid parameter. The Hartman number has significant influence on the temperature distribution as shown in Fig. 11. The findings indicate that the temperature curves improve with increasing values of the Hartmann number. Physically, the rise in temperature within the boundary layer flow as the Hartmann number upsurges is due to Joule heating phenomenon, this leads to the dissipation of energy in the form of heat, causing an increase in the temperature of the fluid. Fig. 12 describes the influence of dimensionless stream-wise coordinate on temperature profile. The plot spectacles that the increasing inputs of stream-wise coordinate slightly rise the temperature curves. Fig. 13 shows the significance of the Prandtl number on the temperature distribution. An increase in the Prandtl number corresponds to a decrease in the thermal diffusivity of the fluid, therefore lower thermal diffusivity suppresses the temperature curves. The Eckert number has major influence on temperature profile and to reveal this impact, we have plotted Fig. 14. Form this plot it is concluded that the Eckert number is responsible for amplification in the temperature curve. Physically, the temperature rise in the boundary layer flow, as the Eckert

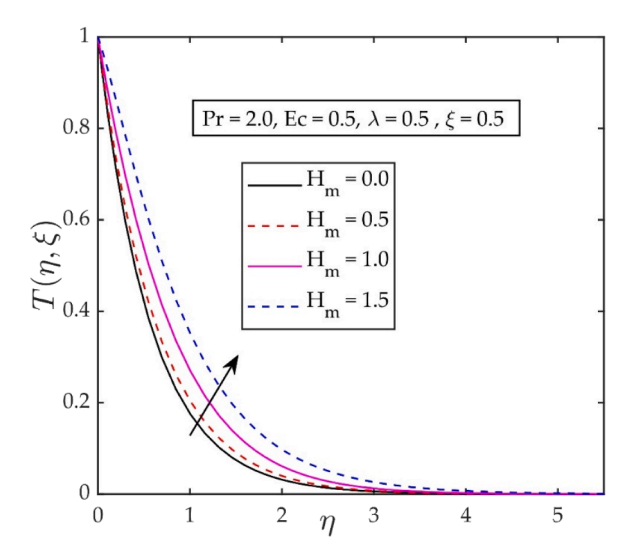


Fig. 11. Impact of Hartmann number H_m on the temperature distribution.

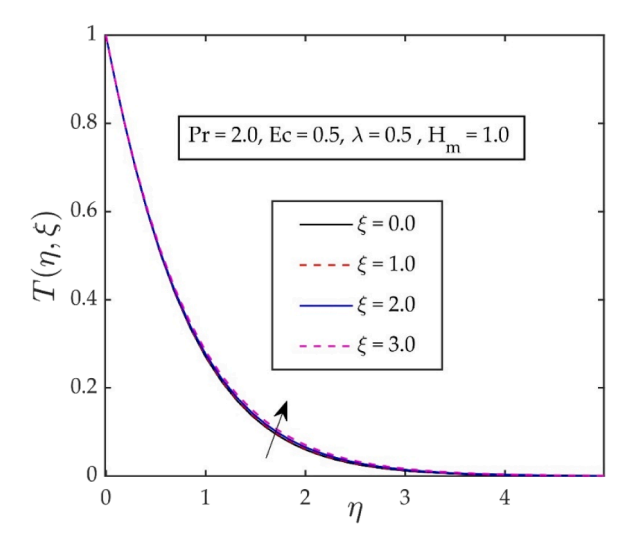


Fig. 12. Impact of dimensionless stream-wise coordinate ξ on the temperature distribution.

number increases, is a result of the conversion of the fluid's kinetic energy into thermal energy. As the Eckert number rises, the fluid's kinetic energy becomes more prominent, resulting in a temperature increase caused by the dissipation of the kinetic energy.

5. Concluding remarks

The non-similar boundary layer flow of the Eyring–Powell fluid, accompanied by thermal analysis under the influence of a uniform magnetic field and viscous dissipation, is examined. The absence of self-similar solutions arises due to the dependence of the fluid parameter on the streamwise spatial coordinate x. Through the incorporation of suitable dimensionless transformations into the governing model, a system of dimensionless and highly nonlinear PDEs is derived. Utilizing the OMD-BSLLM, numerical outcomes are obtained. The sparse matrix obtained through overlapping grid approach can offer computational and memory advantages, providing insights into the underlying structure of a system or problem, and influence algorithm design and matrix properties such as the condition number. The well-conditioned nature of the coefficient matrices with low condition numbers leads to computationally efficient, more stable, accurate and reliable numerical algorithms including the overlapping grid-based spectral collocation method. The subsequent findings from the investigation are emphasized:

• Equations that govern the flow of Eyring-Powell fluid induced by a linear stretching sheet are not self-similar.

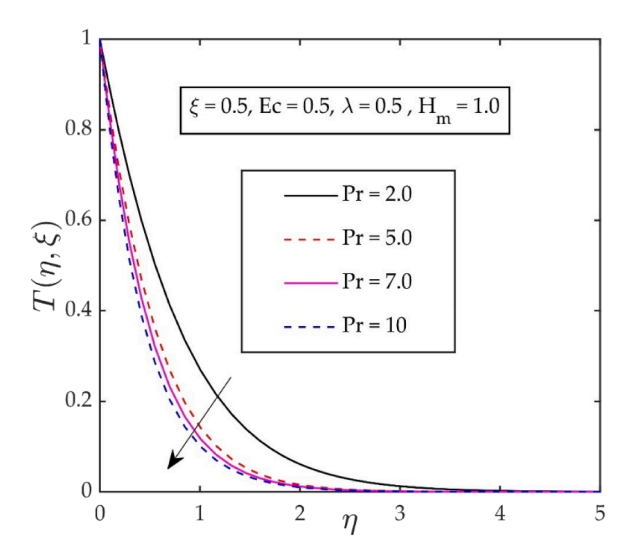


Fig. 13. Impact of Prandtl number Pron the temperature distribution.

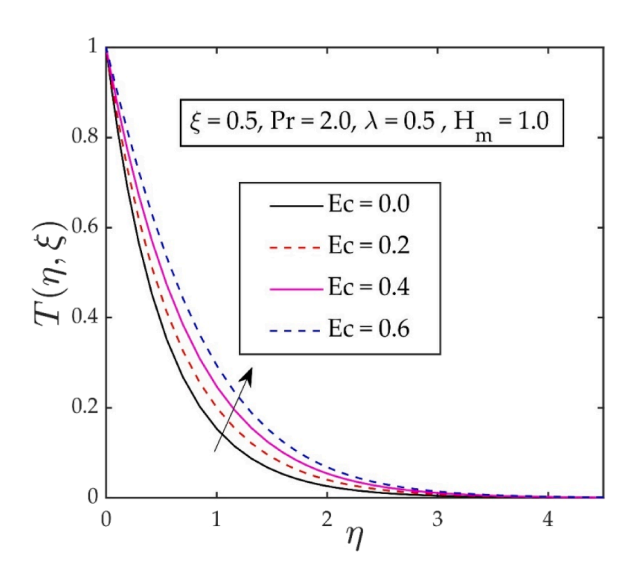


Fig. 14. Impact of the Eckert number Econ the temperature distribution.

- Incrementing in fluid parameter λ and Hartmann number H_m show decrement in skin friction, while inverse results are observed with increasing dimensionless stream-wise coordinate ξ .
- The increment in fluid parameter λ , Hartmann number H_m , dimensionless stream-wise coordinate ξ and Eckert number Ec produce enhancement in Nusselt number, whereas inverse results are found with increasing Prandtl number Pr.
- The temperature curves exhibit enhancement as the dimensionless fluid parameter λ , stream-wise coordinate ξ , Eckert number Ec, and Hartmann number H_m increase. Conversely, a decrease in the temperature curve is observed as the values of Prandtl number Pr improve.
- Increment in fluid parameter, accelerates the fluid whereas deceleration is observed with rising values of Hartmann number and dimensionless stream-wise coordinate.

CRediT authorship contribution statement

Muhammad Idrees Afridi: Writing – review & editing, Writing – original draft, Visualization, Validation, Methodology. M.P. Mkhatshwa: Writing – review & editing, Writing – original draft, Validation, Software, Methodology. Muhammad Qasim: Writing – review & editing, Writing – original draft, Supervision, Project administration, Investigation. Ali J. Chamkha: Writing – review & editing, Writing – original draft, Software, Project administration, Investigation, Formal analysis.

Declaration of competing interest

The authors declare that they have no known competing financial interests or personal relationships that could have appeared to influence the work reported in this paper.

Acknowledgements

The first author would like to express his sincere gratitude to Hanjiang Normal University for their generous support and resources that significantly contributed to the completion of this research.

References

- [1] G. Astarita, G. Marrucci, Principles of Non-Newtonian Fluid Mechanics, McGraw Hill, 1974.
- [2] A.P. Deshpande, J.M. Krishnan, P.B. Sunil Kumar, Rheology of Complex Fluids, Springer, 2010.
- [3] R.P. Chhabra, J.F. Richardson, Non-Newtonian Flow; Fundamentals and Engineering Application, Butterworth-Heinemann, 1999.
- [4] F. Irgens, Rheology and Non-Newtonian Fluids, Springer, 2013.
- [5] A. Wu, Rheology of Paste in Metal Mines, Springer, 2022.
- [6] R. Ellahi, The effects of MHD and temperature dependent viscosity on the flow of non-Newtonian nanofluid in a pipe: analytical solutions, Appl. Math. Model. 37 (2013) 1451–1467.
- [7] M.M. Bhatti, A. Zeeshan, R. Ellahi, O. Anwar Bég, A. Kadir, Effects of coagulation on the two-phase peristaltic pumping of magnetized Prandtl biofluid through an endoscopic annular geometry containing a porous medium, Chin. J. Phys. 58 (2019) 222–234.
- [8] J. Prakash, D. Tripathi, N. Akkurt, O.A. Bég, Tangent hyperbolic non-Newtonian radiative bioconvection nanofluid flow from a bi-directional stretching surface with electro-magneto-hydrodynamic, Joule heating and modified diffusion effects, Eur. Phys. J. Plus 137 (2022) 472.
- [9] J. Prakash, D. Tripathi, A.K. Tiwari, A.K. Pandey, Melting heat transfer and irreversibility analysis in Darcy-Forchheimer flow of Casson fluid modulated by EMHD over cone and wedge surfaces, Therm. Sci. Eng. Progr. 52 (2024) 102680.
- [10] M. Gnaneswara Reddy, D. Tripathi, O. Anwar Beg, Analysis of dissipative non-Newtonian magnetic polymer flow from a curved stretching surface with slip and radiative effects, Heat Transf. 52 (2023) 2694–2714.
- [11] A. Kumar, A. Bhardwaj, D. Tripathi, Bingham plastic fluids flow analysis in multimembranes fitted porous medium, Chin. J. Phys. 90 (2024) 446-462.
- [12] H. Vaidya, D. Tripathi, F.M. Oudina, C. Rajashekhar, H.M. Baskonus, K.V. Prasad, Scrutiny of MHD impact on Carreau Yasuda (CY) fluid flow over a heated wall of the uniform micro-channel, Chin. J. Phys. 87 (2024) 766–781.
- [13] B. Reddappa, R. Geetha, Effects of second order chemical reaction on MHD forced convection Cu, Ag, and Fe₃O₄ nanoparticles of Jeffrey Nanofluid over a moving plate in a porous medium in the presence of heat source/sink, J. Integrat. Sci. Technol. 12 (3) (2024) 762.
- [14] R.E. Powell, H. Eyring, Mechanisms for the relaxation theory of viscosity, Nature 154 (1944) 427-428.
- [15] H.K. Yon, A.J. Ghaiar, A note on Powell-Eyring fluid model, Int. Commun. Heat Mass Transf. 14 (1987) 381–390.
- [16] Ambreen A. Khan, G. Fatima, Sadiq M. Sait, R. Ellahi, Electromagnetic effects on two-layer peristalsis flow of Powell–Eyring nanofluid in axisymmetric channel, J. Therm. Analy. Calorim. 149 (2024) 3631–3644.
- [17] T. Javed, N. Ali, Z. Abbas, M. Sajid, Flow of an Eyring-Powell non-newtonian fluid over a stretching sheet, Chem. Eng. Commun. 200 (2013) 327–336.
- [18] T. Hayat, Z. Iqbal, M. Qasim, S. Obaidat, Steady flow of an Eyring Powell fluid over a moving surface with convective boundary conditions, Int. J. Heat Mass Transf. 55 (2012) 1817–1822.
- [19] M. Qasim, Soret and Dufour effects on the flow of an Erying-Powell fluid over a flat plate with convective boundary condition, Eur. Phys. J. Plus 129 (2014) 24.
- [20] M. Farooq, A. Anjum, S. Rehman, M.Y. Malik, Entropy analysis in thermally stratified Powell-Eyring magnesium-blood nanofluid convection past a stretching surface, Int. Commun. Heat Mass Transf. 138 (2022) 106375.
- [21] J. Rahimi, D.D. Ganji, M. Khaki, Kh. Hosseinzadeh, Solution of the boundary layer flow of an Eyring–Powell non-Newtonian fluid over a linear stretching sheet by collocation method, Alexand. Eng. J. 56 (2017) 621–627.
- [22] W. Ibrahim, T. Lamesse, Powell-Eyring nanofluid analysis with finite element method when past stretching sheet with convective heating and passive control of nanoparticle, Int. J. Thermofluid. 19 (2023) 100388.
- [23] K. Vafai, Ambreen A. Khan, G. Fatima, Sadiq M. Sait, R. Ellahi, Dufour, Soret and radiation effects with magnetic dipole on Powell-Eyring fluid flow over a stretching sheet, J. Num. Method. Heat Fluid Flow 31 (2021) 1085–1103.
- [24] Ambreen A. Khan, Iqra Saleem, R. Ellahi, Sadiq M. Sait, K. Vafai, On magnetohydrodynamics Powell–Eyring fluid with Cattaneo–Christov heat flux over a curved surface, Int. J. Mod. Phys. B 37 (2023) 2350190.
- [25] M. Jalil, S. Asghar, S.M. Imran, Self-similar solutions for the flow and heat transfer of Powell-Eyring fluid over a moving surface in a parallel free stream, Int. J. Heat Mass Transf. 65 (2013) 73–79.
- [26] A.A. Avramenko, M.M. Kovetskaya, I.V. Shevchuk, Self-similar analysis of Eyring–Powell fluid in boundary layer without simplification, Chin. J. Phys. 75 (2022)
- 28–37.
 [27] A. Pantokratoras, Discussion: "Computational analysis for mixed convective flows of viscous fluids with nanoparticles" (Farooq, U., Lu, D. C., Ahmed, S., and
- Ramzan, M., 2019, ASME J. Therm. Sci. Eng. Appl., 11(2), p. 021013), J. Therm. Sci. Eng. Applic. 11 (2019) 055503.

 [28] A. Bisht, R. Sharma, Non-similar solution of Casson nanofluid with variable viscosity and variable thermal conductivity, Int. J. Num. Method. Heat Fluid Flow 22 (2020) 3919–3938.
- [29] R. Razzaq, U. Farooq, Non-similar forced convection analysis of Oldroyd-B fluid flow over an exponentially stretching surface, Adv. Mech. Eng. 13 (2021) 168781402110346.
- [30] M.I. Afridi, Z.M. Chen, N. Riaz, M. Qasim, Heat transfer and flow analysis over a linearly stretching sheet with constant wall temperature: novel local non-similar solutions in the presence of viscous heating, J. Appl. Math. Mech. 103 (2023) e202300003.
- [31] M.I. Afridi, Z.M. Chen, M. Qasim, Entropy generation in local non-similar dissipative MHD flow of CH₃OH + Fe₃O₄ and C₁₂H₂₆-C₁₅H₃₂ + Fe₃O₄ ferrofluids, J. Magnet. Magnet. Mater. 586 (2023) 171177.
- [32] J. Cui, F. Azam, U. Farooq, M. Hussain, Non-similar thermal transport analysis in entropy optimized magnetic nanofluids flow by considering effective Prandtl number model with melting heat transfer and Joule heating, J. Magnet. Magnet. Mater. 567 (2023) 170331.
- [33] R. Razzaq, U. Farooq, Non-similar analysis of MHD hybrid nanofluid flow over an exponentially stretching/shrinking sheet with the influences of thermal radiation and viscous dissipation, Num. Heat Transf., Part B: Fundam. (2024), https://doi.org/10.1080/10407790.2024.2312958.
- [34] U. Farooq, A. Jan, M. Hussain, Impact of thermal radiations, heat generation/absorption and porosity on MHD nanofluid flow towards an inclined stretching surface: Non-similar analysis, J. Appl. Math. Mech. 104 (2024) e202300306.
- [35] M.I. Afridi, A. Wakif, M. Qasim, A.J. Chamkha, A generalized differential quadrature approach to the modelling of heat transfer in non-similar flow with nonlinear convection, Int. Commun. Heat Mass Transf. 155 (2024) 107508.
- [36] M.W. Ahmad, T. Hayat, A. Alsaedi, S.A. Khan, Non-similar solutions for radiative bioconvective flow with Soret and Dufour impacts, Case Stud. Therm. Eng. 53 (2024) 103873.
- [37] Q. Zaman, S. Saleem, N. Ali, Non-similar stagnation flow of Williamson fluid over an isothermal linearly stretched sheet, Num. Heat Transf., Part A: Applic. 85 (2024) 1535–1551.

- [38] E.M. Sparrow, H. Quack, C.J. Boerner, Local non-similarity boundary-layer solutions, AIAA J. 8 (1970) 1936–1942.
- [39] M.I. Afridi, ZM. Chen, T.E. Karakasidis, M. Qasim, Local non-similar solutions for boundary layer flow over a nonlinear stretching surface with uniform lateral mass flux: utilization of third level of truncation, Mathematics 10 (2022) 491.
- [40] M. Mushtaq, S. Asghar, M.A. Hossain, Mixed convection flow of second grade fluid along a vertical stretching flat surface with variable surface temperature, Heat Mass Transf. 43 (2007) 1049–1061.
- [41] D. Srinivasacharya, O. Surender, Non-similar solution for natural convective boundary layer flow of a nanofluid past a vertical plate embedded in a doubly stratified porous medium, Int. J. Heat Mass Transf. 71 (2014) 431–438.
- [42] G. Revathi, P. Saikrishnan, A. Chamkha, Non-similar solutions for unsteady flow over a yawed cylinder with non-uniform mass transfer through a slot, Ain Sham. Eng. J. 5 (2014) 1199–1206.
- [43] M.P. Mkhatshwa, Overlapping grid spectral collocation approach for electrical MHD bioconvection Darcy-Forchheimer flow of a Carreau-Yasuda nanoliquid over a periodically accelerating surface, Heat Transf. 51 (2022) 1468–1500.
- [44] M.P. Mkhatshwa, M. Khumalo, Double diffusion and Hall effects on MHD sinusoidal natural convection flow of silver water-based nanofluid from a porous vertical plate, Part. Different. Equ. Appl. Math. 7 (2023) 100516.
- [45] M.P. Mkhatshwa, Overlapping grid-based spectral collocation technique for bioconvective flow of MHD Williamson nanofluid over a radiative circular cylindrical body with activation energy, Computation 12 (4) (2024) 75, https://doi.org/10.3390/computation12040075.
- [46] V.M. Magagula, On the multidomain bivariate spectral local linearisation method for solving systems of nonsimilar boundary layer partial differential equations, Int. J. Math. Math. Sci. 6423294 (2019) 1–18, 2019.
- [47] M.P. Mkhatshwa, S.S. Motsa, MS. Ayano, P. Sibanda, MHD mixed convective nanofluid flow about a vertical slender cylinder using overlapping multi-domain spectral collocation approach, Case Stud. Therm. Eng. 18 (2020) 100598.
- [48] S.S. MP Mkhatshwa, SS Motsa, P. Sibanda, Overlapping multi-domain spectral method for MHD mixed convection slip flow over an exponentially decreasing mainstream with non-uniform heat source/sink and convective boundary conditions, Int. J. Comput. Method. 18 (2021) 2150004.
- [49] L.N. Trefethen, Spectral Methods in MATLAB, SIAM, Philadelphia, PA, 2000.
- [50] C. Canuto, M.Y. Hussaini, A. Quarteroni, T.A. Zang, Spectral Methods in Fluid Dynamics, Springer, Berlin, 1988.